nature communications

Article

https://doi.org/10.1038/s41467-024-53435-7

# Crustal melting and continent uplift by mafic underplating at convergent boundaries

Received: 5 December 2023

Accepted: 11 October 2024

Published online: 19 October 2024

Check for updates

Zhipeng Zhou [1,2,3], Hans Thybo [1,2,3] ✉, Irina M. Artemieva [1,3,4] ✉, Timothy Kusky [3,5] & Chi-Chia Tang [6]

The thick crust of the southern Tibetan and central Andean plateaus includes high-conductivity, low-velocity zones ascribed to partial melt. The melt origin and effect on plateau uplift remain speculative, in particular if plateau uplift happens before continental collision. The East Anatolian Plateau (EAP) has experienced similar, more recent uplift but its structure is largely unknown. Here we present an 80 km deep geophysical model across EAP, constrained by seismic receiver functions integrated with interpretation of gravity data and seismic tomographic, magnetotelluric, geothermal, and geochemical models. The results indicate a 20 km thick lower crustal layer and a 10 km thick mid-crustal layer, which both contain pockets of partial melt. We explain plateau uplift by isostatic equilibration following magmatism associated with roll-back and break-off of the Neo-Tethys slab. Our results suggest that crustal thickening by felsic melt and mafic underplate are important for plateau uplift in the EAP, Andes and Tibet.

The presence of partial melt within the crust of the southern Tibetan and central Andean plateaus is inferred from low seismic velocities and low electrical resistivity[1–9]. Despite similarity in geophysical observations, the origin and dynamics of the crustal partial melt are attributed to different processes in the two plateaus. Models include partial melting due to crustal thickening in the Tibetan Plateau[2] and by intrusion of asthenospheric material in the central Andes[10]. The timing and cause of plateau uplift and crustal thickening remain controversial, and non-uniqueness of interpretations of crustal structure has contributed to competing geodynamic models. The rise of the Tibetan Plateau has been attributed to underthrusting of Indian lower crust[11], oblique subduction of lithospheric blocks within the plateau[12], and lateral crustal flow[13,14]. In the central Andes, the removal of dense mantle lithosphere and the addition of magma to the lower and middle crust are proposed to promote plateau uplift[10,15].

The uplift of the Gangdese Arc in the Lhasa Block of the Tibetan Plateau began >60 Ma[16,17], predating continent-continent collision[18], and the central Andean Plateau has been uplifting for 23 Myr[19]. The long uplift history of these plateaus introduces challenges in inferring their deep structure at the onset of uplift. Therefore, processes leading to the initiation of plateau uplift may better be studied at young collisional plateaus. The uplift of the East Anatolian Plateau (EAP) in Turkey with a topography of ~1.5–2.0 km began around 12 Ma in relation to the collision between the Arabian Plate and Eurasia[20] with a current convergence rate of 20–30 mm/yr[21].

The EAP has very low Vs anomaly (around −6 to −9% with respect to regional average) in the uppermost mantle[22,23], low Pn velocity (generally Vp < 8.0 km/s and some zones have Vp < 7.8 km/s)[24,25], and high lithosphere temperature (800–900 °C at Moho)[26]. It is broadly covered by Neogene to Quaternary volcanic rocks[27,28]. Dynamic support of the plateau by upwelling asthenosphere has been proposed[29] based on the assumption of a 38–46 km thick crust, as indicated by low-frequency ($f \approx 0.72$ Hz) Receiver Function (RF) studies, which interpret a strong P-wave converter as the Moho under the assumption of constant average crustal Vp/Vs = 1.73 throughout the region[30]. This assumption of constant Vp/Vs ratio contradicts seismic tomography

[1]SinoProbe Lab, Chinese Academy of Geological Sciences, 100037 Beijing, China. [2]Eurasia Institute of Earth Science, Istanbul Technical University, 34469 Istanbul, Turkey. [3]GPMR State Key Lab, School of Earth Sciences, China University of Geosciences, Wuhan 430074, China. [4]Section of Marine Dynamics, GEOMAR Helmholtz Center for Ocean Research, 24148 Kiel, Germany. [5]Center for Global Tectonics and Badong National Observation and Research Station of Geohazards, China University of Geosciences, Wuhan 430074, China. [6]School of Geophysics and Geomatics, China University of Geosciences, Wuhan 430074, China. ✉e-mail: h.thybo@gmail.com; iartemieva@gmail.com

https://doi.org/10.1038/s41467-024-53435-7

models which include significant low-velocity bodies, especially in the active volcanic provinces[22,23], suggesting the presence of intra-crustal, partially molten zones. These zones would require high crustal Vp/Vs and should also produce strong P-RF converters at their base, which easily would be mistaken for the seismic Moho.

Here we apply a refined method[31] for imaging the crustal structure of the EAP by seismic RF. We combine data from a temporary deployment of seismic stations at ~50 km interval[32] and permanent stations from the Kandilli Observatory across the EAP (Fig. 1 and Supplementary Table 1). Our 450 km long RF profile extends from N to S across the EAP in its central part with abundant volcanic fields, the Bitlis Suture, and the northern part of the Arabian Plate. We image strong and weak P-RF converters, and we apply a new gravity-based interpolation method to identify the Moho (Methods)[31]. We demonstrate that the base of the zone that includes partially molten bodies was earlier interpreted as the Moho[30]. To reduce the bias in our interpretation of the RF results, we constrain the upper 80 km of the lithosphere by integrating the RF results with regional seismic tomography[22,23,33,34], magnetotelluric[35], geothermal[26] and geochemical models[27].

## Results

### Crustal receiver function profile

Our P-wave RF model (Fig. 2a) shows the following:

1. The Arabian Plate has a crustal thickness of 35–40 km, as identified by a strong converter in an otherwise non-converting environment.
2. Shallow positive converters close to the margin of the Arabian Plate mark a main detachment which we interpret as the Main Bitlis Thrust (MBT) at a depth of 10–15 km. This blind thrust[36] shares strong similarity to the Main Himalaya Thrust in Nepal[11,37,38].
3. The Bitlis Massif to the south of the Muş Suture has a crustal thickness of ~40 km, with a gradually N-dipping Moho converter (M2) to ~50 km depth in the EAP.
4. The EAP includes two positive converters: M1 at ~30 km and M2 at ~50 km depth (Fig. 2a and Supplementary Table 1). Typically, M1 has larger amplitude than M2 (Supplementary Fig. 1). Additionally, we observe a strong negative converter TL which is located ~10 km shallower than M1 within the EAP. These sub-horizontal converters are observed on all stations within the EAP and are not identified outside the EAP.

The crustal layer between TL and M1 has a very high Vp/Vs ratio of ~2.0 and a low Vs velocity ranging from 2.9 to 3.1 km/s based on calculations of synthetic RFs (Fig. 2b and Supplementary Fig. 2). Results from inverting the RFs for velocities also suggest a low Vs of 2.96-3.33 km/s except for station CMCY in northern EAP (Fig. 3a, Supplementary Figs. 3 and 4). The lower layer between M1 and M2 has a high P-wave velocity (Vp~7.2 km/s) and a high Vp/Vs ratio (~2.0) in its lower part (Fig. 2b).

### Other geophysical observations

We use the long-wavelength filtered Bouguer anomaly for resolving the density contrast across the Moho and for regional scale isostatic calculations, whereas the resolution of the gravity data (~9 km laterally[39]) may be too low to model the dimensions of individual melt

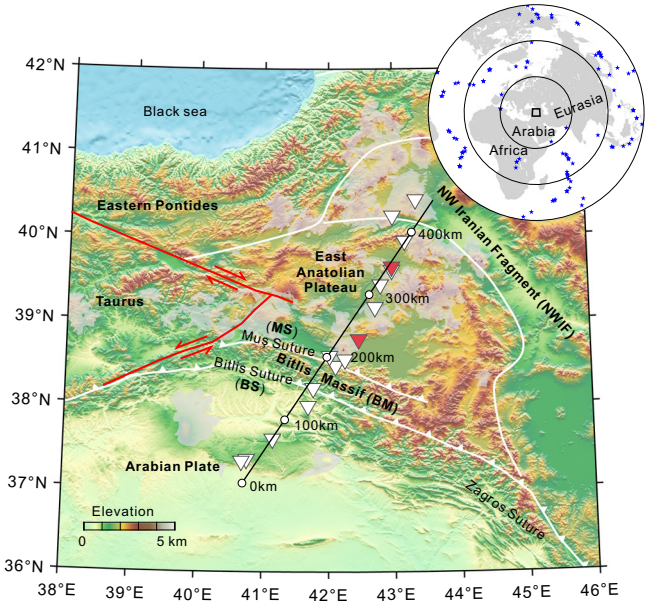


**Fig. 1 | Topographic map and tectonic setting of the East Anatolian Plateau (EAP).** Main map: regional topography; grey transparent shading—Neogene to Quaternary volcanics; inverted triangles—seismic stations used in this study, red inverted triangles—stations used for illustrated receiver functions with synthetic tests (Fig. 2b); thick black line—location of receiver function profile; white lines—collisional structures with subduction direction marked by white triangles, except for zones with controversal subduction direction[29,67,68]; red lines with arrows —large strike-slip faults. Insert: geographical location of the study area with blue stars showing epicentres of teleseismic events used for the calculation of RFs.

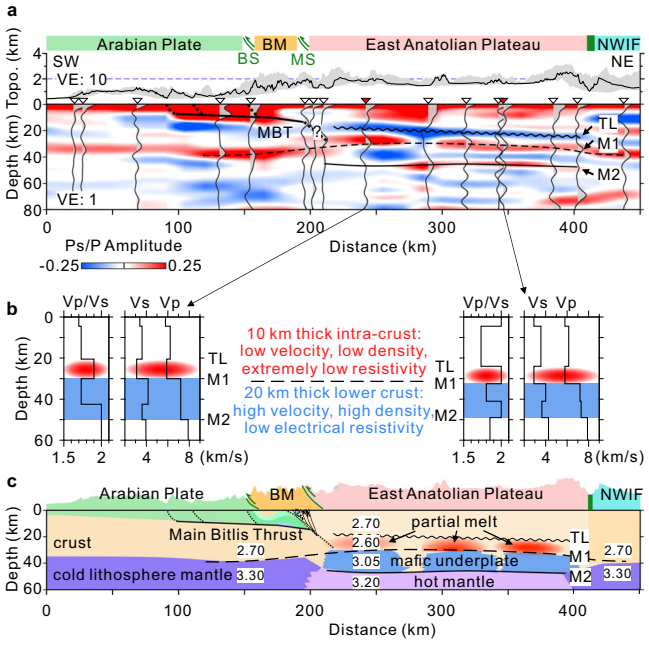


**Fig. 2 | Receiver Function (RF) profile across the East Anatolian Plateau (EAP).** **a** Depth-migrated RF profile (red and blue colors represent increase and decrease of seismic impedance with depth, respectively). Black line atop RFs shows topography along the profile and its variation within a ± 40 km-wide corridor (grey shading). Color boxes at the top mark four tectonic units (BM – Bitlis Massif, NWIF – NW Iranian Fragment) separated by suture zones (BS – Bitlis Suture, MS – Muş Suture). Inverted triangles show the locations of seismic stations. Grey wiggly lines are the stacked RFs at each station migrated to depth. TL and M1 converters surround a ~ 10 km thick intra-crustal low-velocity zone, M1 is the previously interpreted RF Moho[30,45], which we interpret as the top of a mafic layer above our interpreted Moho M2. **b** Crustal velocity models for two stations (red triangles in **a**) based on modelling with synthetic RFs (Supplementary Fig. 2). The ~10 km thick low-velocity intra-crustal zone (red color) has an electric resistivity of 1 Ωm[35] and a density of 2.60 g/cm$^3$; and the ~20 km thick lower crust has an electric resistivity of 10–30 Ωm[35] and a density of 3.05 g/cm$^3$. **c** Sketch of our interpretation. Numbers are density in g/cm$^3$ constrained by gravity modeling (Supplementary Fig. 5b). Solid line M2 – the interpreted Moho, dashed line M1 – top of mafic underplate.

https://doi.org/10.1038/s41467-024-53435-7

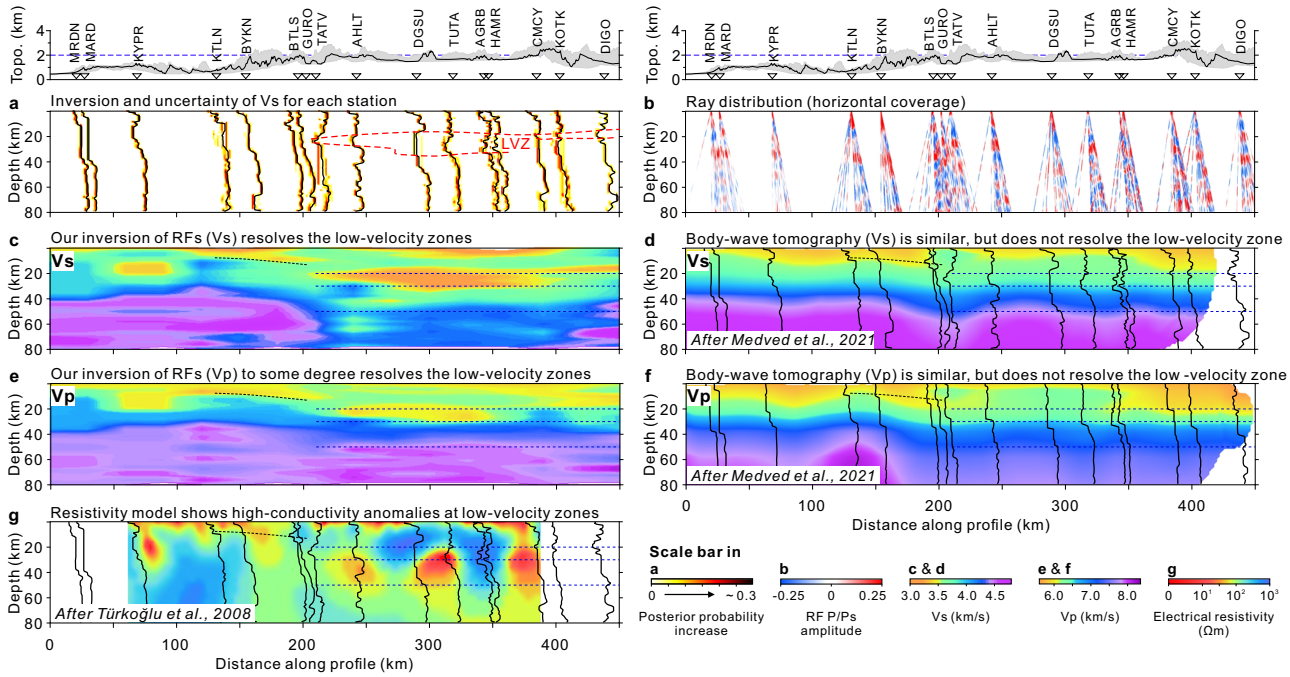


**Fig. 3 | Seismic and electrical structure along the RF profile.** Plot on the top – topographic profile within a ± 40 km-wide corridor along the profile, seismic stations are shown by inverted triangles with code names on the top. **a** Vertical Vs profiles at each station from non-linear inversion[63] of RF (cf. Methods and Supplementary Figs. 3, 4). Probablity scale originates from the inversion algorithm, cf. Supplementary Fig. 3. Dashed lines contour the intra-crustal low-velocity zone (LVZ) at the EAP, interpreted to include bodies of partial melt. **b** Migrated RF at individual stations displayed in the depth domain to show the data coverage of the profile. **c**, **e** P- and S-wave models obtained by interpolation of our velocity inversion results in (**a**). **d**, **f** Seismic tomographic S- and P-wave models[33]. Superimposed vertical profiles show the individual velocity profiles from our velocity inversion. **g** Electrical resistivity structure[35] with Vs from our RF inversion superimposed. Notice the correlation between low-resistivity bodies and low-velocity zones.

pockets. A body wave travel time tomographic velocity model[33] shows that the crustal layer between M1 and M2 (30–50 km depth) in the EAP has a Vp velocity between 6.6 and 7.2 km/s (Fig. 3f). Gravity modeling (Supplementary Fig. 5b) suggests that the layer between M1 and M2 has a high density of 3.05 g/cm$^3$, assuming a density of 3.20 g/cm$^3$ in the hot uppermost mantle at 50-70 km depth (Fig. 2c). This layer also includes several bodies with low electrical resistivity of 10–30 Ωm[35] (Fig. 3g).

The low-velocity anomaly between TL and M1 (20–30 km depth) cannot be clearly resolved by body wave tomography due to vertical resolution limitations[33]. It is, however, observed in Rayleigh wave data at a period of 30 s[22]. Strong low-density (2.60 g/cm$^3$, Fig. 2 and Supplementary Fig. 5b) and low-resistivity (~1 Ωm) zones[35] (Fig. 3g) are unique for the EAP in the study region. The converters TL, M1, and M2 along with magnetotelluric anomalies are only observed in the volcanic province of the EAP, which has 0.5–1.0 km higher topography than neighboring blocks (Fig. 3).

## Crustal converters and the presence of magma

The parameters of the layer between TL and M1 (~1 Ωm electric resistivity[35], Vs~3.0 km/s[22], and Vp/Vs ratio ~2.0 at 20–30 km depth) are similar to a layer containing crustal silica melt observed in the central Andes, where joint inversion of surface wave dispersion and RF constrains Vs = 1.9-3.1 km/s[40], with average Vs~3.1 km/s from RF synthetic modelling[3], and electric resistivity lower than 1 Ωm[7,41]. The Vp/Vs value of ~2.0 between TL and M1 indicates a distinct Vs decrease in this layer which may be caused by the presence of either fluids or partial melt. Considering the young magmatic activity in the EAP (Fig. 4a) and the temperature close to the felsic solidus at 30 km depth (Fig. 4b), the presence of pockets with felsic partial melt is the most likely explanation for this depth interval at 20–30 km. Heat flow data are absent along our profile, but the 12–18 km deep Curie temperature depth indicates high heat flow[26]. For a dihedral angle of 20–40° in the equilibrium geometry model, with an aspect ratio of 0.10–0.15[42], we estimate the melt volume fraction by a forward model for partial melting[43] to be between 3 and 13% for a Vs value between 2.96 and 3.33 km/s (Supplementary Fig. S6a).

The MT model (Fig. 3g) indicates the presence of three major, individual melt bodies in the EAP separated by ~70 km, but the resolution of the available data is insufficient to provide measures of their dimension due to leakage of the low-resistivity in the model. The depth to the top of these bodies (~20 km) corresponds to the top (TL) of the upper low-velocity zone (LVZ), which extends continuously across the EAP (Fig. 3c), and the LVZ thickness may indicate the vertical extent of the melt pockets. The receiver functions and the seismic tomographic models have insufficient resolution to outline the individual partially molten bodies, but the recurrent low-velocity zone at all stations in the EAP indicates that the material between TL and M1 generally is close to the solidus[44], also outside the bodies containing partial melt.

Previous RF interpretations selected M1 as the Moho[30,45] because it is the strongest converter in the RF section. By the new method[31] based on long-wavelength gravity-interpolation of converters from the Arabian Plate we, instead, find that the strong converter represents the strong contrast between the low-velocity partially molten layer and the high-velocity (Vp~7.2 km/s) and high-density (~3.05 g/cm$^3$) lower crust, most likely with mafic composition (Supplementary Fig. 5b). The lower part of this layer has a Vp/Vs of ~2.0 and an electric resistivity of 10–30 Ωm[35] which indicates the presence of a, not yet fully solidified, mafic magmatic material. High Vp of ~7.2 km/s is typical for mafic rocks at 1.4 GPa and 900 °C (~50 km depth in the EAP)[43]. This Vp value is lower than in the underplated lower crust with Vp = 7.4-7.6 km/s at the Baikal Rift Zone[46], but it is similar to other underplated layers like in the Kuril Arc, the Norwegian-Danish Basin and the Donbas Basin[47]. It is unlikely that this layer may represent the underthrusted Neo-Tethys oceanic

https://doi.org/10.1038/s41467-024-53435-7

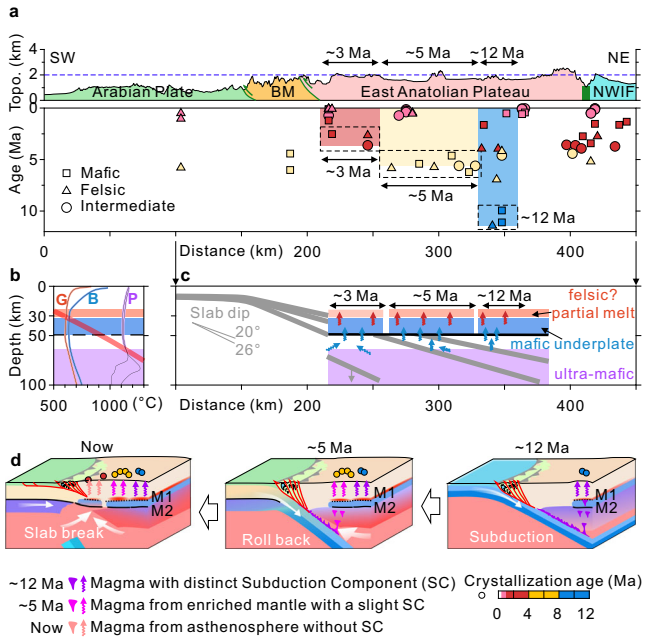


**Fig. 4 | Evolution of magmatic activity along the profile. a** Profile on the top – topography marked with 4 tectonic units (abbreviations as in Fig. 2). Lower diagram - Age of volcanism[28] within a ± 100 km-wide corridor along the RF profile. **b** Regional geotherm (thick red line)[26] and experimental solidi. Line G: for wet felsic rock[49] which suggests partial melting of felsic crust at a depth of ~30 km (pink layer). Line B: for wet mafic rocks[48] which implies partial melting of the crust below 30 km depth (blue layer). Line P: for peridotite with small amount of C-H-O[69,70] which implies mantle melting below 70 km depth (purple layer). **c** Temporal change of subduction slab dip (thick grey lines) from 20° to 26° due to roll-back[27,34]. Blue arrows illustrate migration of fluids and mafic melts extracted from the mantle wedge into the lower crust. Upward migration of fluids and felsic magma together with partial melting due to heat flux (red arrows) create partially molten material in mid-crustal layer (pink color) in the EAP. **d** Geodynamic sketch of the tectonic evolution (from right to left). Colored circles at surface show ages of volcanism. Magma composition[27] is illustrated at depth by colors. Converters M1 (black dotted line) and M2 (black solid line) bound the 20 km thick underplated mafic layer, the red layer above M1 is the zone containing pockets with felsic partial melt.

slab, since tomographic images and geochemical results indicate that the oceanic slab has broken off[27,34].

### Geodynamic evolution and magmatism

Most of the recent magmatism[28] along the profile is concentrated in the EAP with variable magma composition ranging from felsic to mafic and a clear pattern of north to south younging of the onset of magmatic activity since 12 Ma (Fig. 4a and Supplementary Fig. 7). The occurrence of very young magmatism, with age less than 1 Myr, suggests the presence of magma chambers and partially molten bodies within the crust that can still be detected using geophysical data. The predicted geotherms[26] intersect the experimental wet mafic rock solidus[48] at depths of ~30–50 km and cross the wet felsic solidus[49] at a depth of ~30 km (Fig. 4b). This indicates that the mafic lower crust between M1 and M2 at 30 to 50 km depth, especially its lower part with high temperature, may still be partially molten which is consistent with the Vp/Vs of ~2.0. Further, the low velocity zone between TL and M1 at 20–30 km depth probably includes partial melt of felsic composition, considering that the estimated temperature of ~600 °C at a depth of 30 km[26] is below the wet mafic melting solidus, the high Vp/Vs of ~2.0 and the low resistivity of ~1 Ωm.

We explain the lateral change of magmatism from 12 Ma to 3 Ma by spatial changes in subduction dynamics and geometry. Assuming that the subducting Neo-Tethys slab induces melting of the mantle wedge at a depth of ~70 km (Fig. 4c), and observing the magmatism of various ages at distances of 345 ± 15 km (~12 Ma), 295 ± 36 km (~5 Ma), 230 ± 21 km (~3 Ma), the subduction angle would have steepened from 20 ± 1.5° (~12 Ma) to 26 ± 6° (~5 Ma). Alternatively, the magmatism might have been caused by delamination of the lithospheric mantle and lower crust[28,50], but this mechanism does not explain the clear southward younging of magmatism initiation. We propose that underplating[47] (addition of mafic magma to the lower crust or below the original Moho) led to magma fractionation and that the accompanying release of fluid and heat initiated melting of preexisting continental crust, which may explain the presence of the mid-crustal partially molten bodies.

Slab roll-back and break-off in the EAP have earlier been proposed based on geochronology, geochemistry and seismic tomography[27,34]. We extend this interpretation by our geophysical model (Fig. 4d), which suggests that the magmatism moved laterally from north to south due to slab roll-back and steepening followed by slab break-off, and that this evolution caused intensive addition of mafic magma to the lower crust and intra-crustal partial melting.

## Discussion

The free air gravity anomaly difference between the Arabian plate and EAP, of about 30-40 mGal, implies that the topography is mainly controlled by isostatic buoyancy (Supplementary Fig. 8). Compared to the Arabian plate, the EAP has an additional elevation of ~0.75 km. Selecting the 1 km topography in the Arabian plate as reference, our new seismic-density model (Fig. 2c) explains the actual topography of the EAP by isostasy for a density of 3.3 g/cm$^3$ in the mantle lithosphere and 3.2 g/cm$^3$ in the asthenosphere (Fig. 5a, Supplementary Fig. 8a).

The presence of a 20 km thick layer containing high-velocity, mafic material in the EAP is not unique. A similar size (~200 km long and ~20 km thick) high-velocity lower crust has been also mapped by RF below the central Andean plateau[3,10] (Fig. 5b) and in parts of the Lhasa Block of the Tibetan plateau[11] (Fig. 5c). The free air gravity anomalies in the central Andean plateau and the Lhasa block are up to ~90 mGal and ~40 mGal, respectively. We calculate the isostatic topography by adding the necessary small corrections for the isostatic equivalent of the free air anomalies (Fig. 5bc, Methods and Supplementary Fig. 8). The results indicate that isostasy is the primary cause of the topography.

In the central Andean Plateau, our model predicts the observed topography with the same densities of 2.60 g/cm$^3$ for the layer with partially molten bodies and 3.05 g/cm$^3$ for the underplated lower crust as in the EAP. For the southern Tibetan Plateau, two end-member models for the thickness of the upper to middle crustal layer with partially molten bodies have been proposed: either (1) it is thick and the continuation of a seismic "bright spot" downward to the top of mafic lower crust[2] or (2) it is limited to only 10 km thickness[11]. Although model 1 now appears unrealistic, we consider both models for the Tibetan Plateau, where the observed topography may be fit by densities of 3.30 g/cm$^3$ or 3.15 g/cm$^3$ in the lower crust for the two end-member models, respectively (Fig. 5c). This indicates that the mafic lower crust may be partially metamorphosed into eclogite: Eclogitization may be caused by the very deep level of the lower crust in Tibet (70–80 km)[51–53].

Our observations of the crustal structure of three plateaus in collisional settings with different topography and uplift duration (12 Ma in EAP, 23 Ma in Altiplano, and 60 Ma in Tibet) indicate that (Fig. 6):

1. the high-density, high-velocity mafic lower crust has comparable thicknesses of ~20 km in all three plateaus;
2. the thickness of a mid-crustal layer containing bodies of felsic melt has key influence on plateau elevation, and this thickness

https://doi.org/10.1038/s41467-024-53435-7

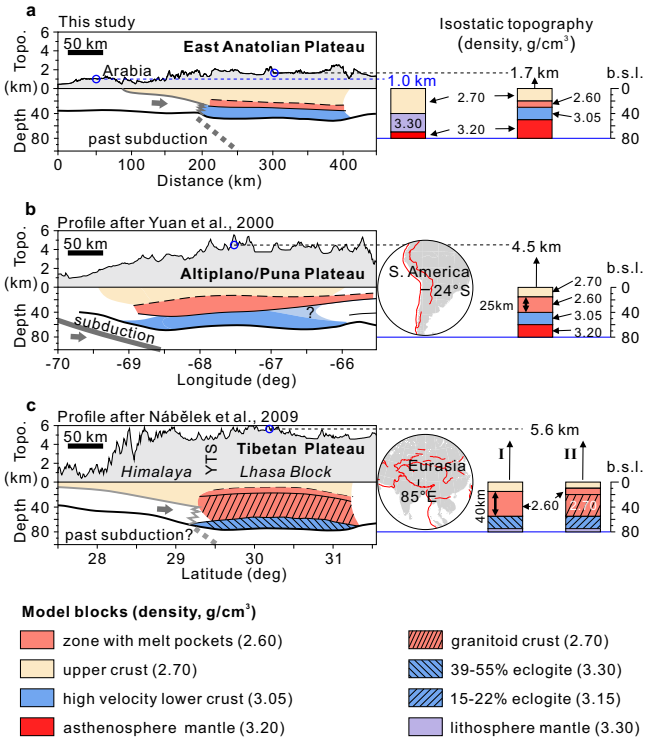


**Fig. 5 | Plateau uplift by underplating and crustal partial melting. a** East Anatolian Plateau, (**b**) central Andes Plateau, (**c**) Tibetan Plateau. Left panels: schematic cross-sections through the three plateaus constrained by regional models with topographic profiles on top. Middle panels in (**b**), **c** profile locations. Right panels – 1D crustal density (in g/cm³) models used for calculating the predicted topography (dotted lines with values on the right) from the free air gravity, assuming isostasy with a compensation depth of 80 km and with the Arabian Plate as reference model (middle panel in (**a**) with 1.0 km topography) (Methods and Supplementary Fig. 8). The predicted elevation for the EAP lithosphere model in Fig. 2c is 1.7 km as observed (**a**). The elevation of 4.5 km in the Altiplano/Puna Plateau (**b**) is explained by a lithosphere model with the same densities as for the EAP, similar thickness of the high-velocity lower crust[3], and the presence of a felsic partially molten crustal body[71]. The high topography of the Lhasa block (**c**) reflects a balance between the degree of lower crust eclogitization[11,52,72] and the thickness of the melt-hosting layer inconclusively imaged seismically with two end-member models. Both models explain the observed 5.6 km high topography. Model I[2] has a 40 km thick layer (with bulk 2.60 g/cm³) hosting partially molten bodies and a 20 km thick eclogitic lower crust (3.30 g/cm³, with 39–55% eclogitization). Model II[11] has a 10 km thick layer with partially molten bodies, above a lower crustal layer with density of 3.15 g/cm³ (15–22% eclogitization).

appears positively correlated with the duration of uplift and the present plateau elevation.

3. crustal thickness increases through the growth of the mid-crustal layer.

The case of the central Andes shows that continent-continent collision is not required for plateau uplift, and the uplift of the Altiplano plateau is consistent with the recent observation of pre-collision uplift of the Gangdese Arc in southern Tibet[18]. For a thin overriding plate, like the Japanese Arc with a ~15 km thick upper crust, neither plateau uplift nor intra-crustal partial melting is observed, but a ~15 km thick mafic lower crust may be present[54]. We speculate that underplating may occur, but the thickness of the continental crust may be insufficient to generate large volumes of felsic magma by crustal melting. However, we find that plateau uplift, where the overriding plate is continental, generally can be explained by mafic underplating in association with intra-crustal partial melting. The final high plateau is built by inflating the weakened, low viscosity continental crust containing bodies of partial melt, while

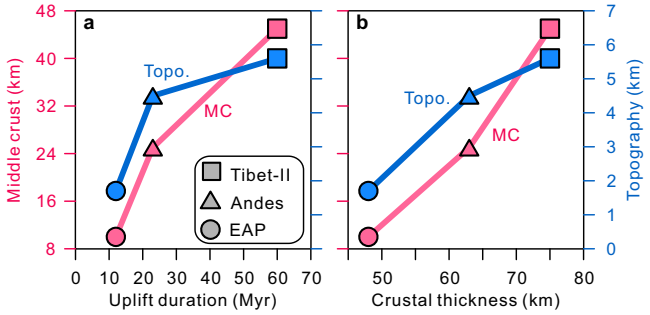


**Fig. 6 | Relation between plateau uplift duration, thickness of the middle crustal layer and crustal thickness in EAP, Andes and Tibet.** The middle crustal layer is defined as the layer between the brittle upper crust and the mafic lower crust. Thickness of the mid-crustal layer and topography versus (**a**) age of plateau uplift and (**b**) crustal thickness.

the uplift-induced regional climate change may affect the high topography and vice-versa[55,56].

Our observations of the physical state of the lithosphere during the initial stage of plateau uplift provide a quantitative framework for the factors that lead to the formation of bodies of a partially molten material within the crust, and their buoyancy effects on continental plateaus are enhanced by mafic underplating of new lower crust[17,57]. Our revised geodynamic understanding of continental uplift explains topographic change at pre-collisional stage[18]. Our results indicate that subduction below continental lithosphere is a necessary condition for collisional thickening by underplating, intra-crustal melting and related plateau uplift, and the process is independent of the nature of the subducting plate.

## Methods

### Receiver functions (RF)

The (radial) Ps RF is calculated by time domain iterative deconvolution by ITERDECON[58] with a Gaussian filter of 2.5, which corresponds to a cut off frequency of ~1.24 Hz. RFs were processed for epicentral distances of 30–90° and each RF from each station has been manually inspected (Supplementary Fig. 9). RFs with a large difference from the overall characteristics of other RFs were rejected in the final RF results. We manually picked the P-wave arrival time of each RF (Supplementary Fig. 9c). For some seismic phases with weak amplitude, we also used the multiple-taper correlation (MTC)[59] to estimate the RFs (Supplementary Fig. 9d); a comparison of the RF results from different deconvolution methods ensures recognition that the weak seismic phases are not noise artifacts. Synthetic RF tests were calculated by the IRFFM (Interactive Receiver Function Forward Modeller) software[60].

Assuming a single-layer medium, the crustal thickness $H$ and the crustal average $\kappa = Vp/Vs$ are determined by $H$-$\kappa$ stacking[61] of the converted Ps wave and the reflected multiples from the Moho interface. We use weight parameters of 0.6, 0.3, 0.1 for the Ps, PpPs, PsPs +PpSs phases to stack the peak amplitudes (Supplementary Fig. 1b). The sensitivity of the results to the assumed constant Vp=6.3 km/s is insignificant within uncertainty (Supplementary Fig. 10). We record all possible $H$-$\kappa$ pairs, and use the gravity field data to determine the final $H$-$\kappa$ values according to a new method[31] (see details in the section on Gravity interpolation of RF results).

RFs were migrated into the depth domain (Figs. 2a, 3b) based on the assumed crustal P-wave velocity of 6.3 km/s, and the Vp/Vs ratio (Supplementary Table 1) retrieved from the $H$-$\kappa$ stacking with application of gravity interpolation of the RFs (Supplementary Fig. 11). The final RF and velocity profiles are obtained by applying a moving average filter with a radius of 30 × 2 km (horizontal × vertical) to the migrated RF rays and the inverted Vp and Vs profiles.

### Velocity inversion of RFs

We estimate vertical P- and S-wave velocity profiles from the RFs by applying three different methods: linear RF inversion[62], non-linear RF inversion by the transdimensional Markov-chain Monte Carlo (MCMC) algorithm[63] and the Neighborhood Algorithm (NA)[64,65]. The results of the non-linear algorithms are similar, including the identification of the low-velocity zones in the middle crust. The first algorithm assumes a constant Vp/Vs = 1.73. We first check that this method leads to similar results as an earlier application for the EAP[30], when constrained to the upper 40 km of the crust. Application of the same method to more realistic depths of 50 and 56 km for detecting the Moho, produces results that include the pronounced low-velocity zone between 20 and 30 km depth as well as a Moho at around 50–60 km depth (Supplementary Fig. 3a). By extending the covered depth interval, the visual fit between calculated and observed RF is substantially improved (Supplementary Fig. 3a).

The non-linear transdimensional MCMC inversion algorithm[63] estimates both Vp and Vs profiles (and thereby Vp/Vs). Given the strong variation in Vp/Vs along the EAP profile, this method provides better resolution of depth and velocity variation, and it leads to a better fit between calculated and observed RF (Supplementary Fig. 3b). The results identify a clear Moho transition in addition to a strong velocity contrast at the base of the mid-crustal layer with partially molten bodies. The determined vertical velocity profiles for individual stations correlate very well between each other along the profile as documented by the velocity profiles (Fig. 3c, e). The resulting vertical Vs profiles also correlate with the occurrences of high-conductivity bodies in the MT model (Fig. 3g). The NA inversion[64,65] identify the same low-velocity zones beneath stations within EAP although the results are less detailed as the NA is restricted to 6 layers in the models (Supplementary Fig. 12). Each inversion included 1000 iterations with 20 models generated at each iteration and 10 Voronoi cells re-sampled at each iteration. The results are consistent with results from the MCMC inversion which confirms that the inverted Vs profiles are robust.

As the inversion was carried out independently for each station, the strong lateral continuity of the resulting vertical velocity profiles testifies to the presence of anomalous bodies (melt pockets) in the same depth interval along the profile, and it justifies the horizontal interpolation of the results between the stations.

### Gravity calculations

The horizontal resolution of ~9 km and the amplitude accuracy of ~9 mGal of the EIGEN-6C4 gravity data[39] may be insufficient for modelling the individual molten bodies in the crust with unknown size. Instead, we use the long wavelength gravity signal for calculation of the isostatic topography and for resolving the density contrast across the Moho. The 2-D gravity forward calculations are made with the FastGrav software. The Bouguer gravity anomaly is calculated for the EIGEN-6C4 gravity data[39] and the ETOPO1 topography data[66], assuming a crustal density of 2.67 g/cm$^3$. To model the gravity signal from a deep Moho, the short-wavelength Bouguer anomaly fluctuations, originating from the shallow crust, are removed with a Gaussian filter of 500 km[31].

Model 1 (Supplementary Fig. 5b) explains the observed gravity anomaly and is consistent with the RF profile. It includes the crustal layer with partially molten bodies (with bulk layer density of 2.60 g/cm$^3$, Vs~3.0 km/s, Vp~6.0 km/s) and the mafic underplated layer (density of 3.05 g/cm$^3$, Vs of 3.6-4.1 km/s, Vp~7.2 km/s) for an asthenosphere density $D_1$ of 3.2 g/cm$^3$. Model 2 without the mid-crustal low-velocity layer and the underplated lower crust (Supplementary Fig. 5c) cannot fit the gravity data unless the density of the asthenosphere beneath the EAP[22] is unrealistically high (>3.3 g/cm$^3$, cf. green line) or the density of the lower crust is high (≥2.95 g/cm$^3$, cf. black line), corresponding to an underplated lower crust, which supports the presence of an underplated lower crustal layer.

### Gravity interpolation of RF results

We apply a new method[31] for regional determination of Moho depth variation by minimizing the difference between the long period gravity signal and potential Moho depths along the profile, selected from the results of $H$-$\kappa$ stacking[31]. The method selects the optimum Moho depth at each seismic station from several possible candidates derived from the $H$-$\kappa$ stacking by testing the crustal models against gravity. We adopt an empirical correlation between regional long-wavelength (>248 km) Bouguer gravity anomaly ($\Delta g_B$) and Moho depth (D), so that a lower value of the Bouguer gravity anomaly corresponds to a deeper Moho: $\Delta g_B = a + bD$, where $a$ and $b$ are empirical regional parameters. For a known $\Delta g_B$, we minimize the difference between the Moho depth obtained as $(\Delta g_B - a)/b$ and multiple Moho candidates from the regional RFs by scanning the $a$, $b$ parameter space. This procedure[31] determines the approximate Moho depth for any given $\Delta g_B$ value, and allows us to select the closest RF Moho depth (Supplementary Fig. 11)[31].

### Predicted topography

To calculate the predicted topography in the three plateaus, we assume regional isostasy with pressure equilibrium at a depth of 80 km below the different tectonic units. The Arabian Plate is close to isostatic equilibrium with a free air (FA) gravity anomaly of ~20 mGal, and we adopt it as reference model. The lithostatic pressure is $P_{ref} = t_o\rho_o + \Sigma h_i\rho_i$, where $t_o$ and $\rho_o$ are thickness and density of the material above sea level, $h_i$ and $\rho_i$ are thickness and density of different layers from sea level to 80 km depth. Isostatic topography for other tectonic units is therefore $t_{iso} = (P_{ref} - \Sigma h_i\rho_i)/\rho_o$. The predicted free air gravity anomaly is $FA = 2\pi G(t_o\rho_o + \Sigma h_i\rho_i)$. At full isostatic equilibrium (and neglecting lithosphere flexure) FA should be near-zero, but the central Andes and Tibet have FA anomalies of ~90 mGal and ~40 mGal, respectively. We assume that the extra $\Delta FA$ anomaly originates from a non-isostastic topography component of $\Delta t = \Delta FA/2\pi G/\rho_o$ in addition to the isostatically predicted topography, $t_{iso,}$with the Arabian Plate adopted as reference. This non-isostatic correction allows for including the observed FA into the isostatic calculation.

### Quantitative comparison with tomography and MT models

Age data of magmatic rocks in Eastern Anatolia[28] within a ± 100 km wide corridor is projected onto the profile (Fig. 4; Supplementary Fig. 7). The absolute P-wave and S-wave velocity profiles[33] are located along the RF profile. The MT model[35] is smoothed by parameters of alpha = 1, tau = 3[35], to compare to the RF result, as these parameters provide the smallest misfit between the magnetotelluric data and the resistivity model[35].

We calculate the P-wave and S-wave velocities at different melt fraction, pressure and temperature by forward modeling[43] of seismic velocity and electrical conductivity and compare with the absolute P- and S-wave velocity profiles[33] and the smoothed resistivity model[35] along the RF profile (Fig. 3; Supplementary Fig. 6).

## Data availability

All data used in this contribution are available as referred to in the main text, supplementary material, source data, and references. The interpreted broadband seismic data originate from the Eastern Turkey Seismic Experiment (ESTE)[32] (available at Incorporated Research Institutions for Seismology, IRIS: https://ds.iris.edu/ds/nodes/dmc) and from Kandilli Observatory, Bogazici University (available at AFAD: https://tdvms.afad.gov.tr/continuous_data) (Supplementary Table 1). Source data are provided with this paper.

## Code availability

The programs used in this research are available online. Programs for RF analysis include: Rftn.Codes packages for time-domain deconvolution and linear inversion of RFs (http://eqseis.geosc.psu.edu/cammon/HTML/RftnDocs/thecodes01.html); Recfunk21 program for

multitaper spectral correlation (https://github.com/RUseismology/Recfunk21); hk1.3 program for H-κ analysis (https://www.eas.slu.edu/People/LZhu/home.html); IRFFM package for visual forward modelling of RF and NA package for RF neighbourhood inversion (http://www.iearth.edu.au/codes); and RF_INV packages for transdimensional Markov-chain Monte Carlo inversion (https://github.com/akuhara/RF_INV). Program used for rock velocity analysis - SEFMO_20210417 (https://agupubs.onlinelibrary.wiley.com/doi/10.1029/2021JB022307); program used for gravity forward modelling - FastGrav (http://fastgrav.com/).

## References


1. Brown, L. D. et al. Bright spots, structure, and magmatism in southern Tibet from INDEPTH seismic reflection profiling. *Science* **274**, 1688–1690 (1996).
2. Nelson, K. D. et al. Partially molten middle crust beneath southern Tibet: synthesis of project INDEPTH results. *Science* **274**, 1684–1688 (1996).
3. Yuan, X. et al. Subduction and collision processes in the Central Andes constrained by converted seismic phases. *Nature* **408**, 958–961 (2000).
4. Wei, W. et al. Detection of widespread fluids in the Tibetan crust by magnetotelluric studies. *Science* **292**, 716–719 (2001).
5. Unsworth, M. J. et al. Crustal rheology of the Himalaya and Southern Tibet inferred from magnetotelluric data. *Nature* **438**, 78–81 (2005).
6. Kind, R. et al. Evidence from Earthquake Data for a Partially Molten Crustal Layer in Southern Tibet. *Science* **274**, 1692–1694 (1996).
7. Unsworth, M. et al. Crustal structure of the Lazufre volcanic complex and the Southern Puna from 3-D inversion of magnetotelluric data: Implications for surface uplift and evidence for melt storage and hydrothermal fluids. *Geosphere* **19**, 1210–1230 (2023).
8. Jin, S. et al. Relationship of the crustal structure, rheology, and tectonic dynamics beneath the Lhasa-Gangdese Terrane (Southern Tibet) Based on a 3-D electrical model. *J. Geophys. Res. Solid Earth* **127**, e2022JB024318 (2022).
9. Huang, S. et al. High-resolution 3-D Shear Wave Velocity Model of the Tibetan Plateau: Implications for Crustal Deformation and Porphyry Cu Deposit Formation. *J. Geophys. Res. Solid Earth* **125**, e2019JB019215 (2020).
10. Perkins, J. P. et al. Surface uplift in the central andes driven by growth of the altiplano puna magma body. *Nat. Commun.* **7**, 13185 (2016).
11. Nábělek, J. et al. Underplating in the Himalaya-Tibet collision zone revealed by the Hi-CLIMB experiment. *Science* **325**, 1371–1374 (2009).
12. Tapponnier, P. et al. Oblique stepwise rise and growth of the Tibet Plateau. *Science* **294**, 1671–1677 (2001).
13. Royden, L. H., Burchfiel, B. C. & van der Hilst, R. D. The geological evolution of the Tibetan Plateau. *Science* **321**, 1054–1058 (2008).
14. Beaumont, C., Jamieson, R. A., Nguyen, M. H. & Lee, B. Himalayan tectonics explained by extrusion of a low-viscosity crustal channel coupled to focused surface denudation. *Nature* **414**, 738–742 (2001).
15. Garzione, C. N. et al. Tectonic evolution of the Central Andean Plateau and implications for the growth of plateaus. *Annu. Rev. Earth Pl. Sc.* **45**, 529–559 (2017).
16. Ding, L. et al. Timing and mechanisms of Tibetan Plateau uplift. *Nat. Rev. Earth Environ.* **3**, 652–667 (2022).
17. Zhu, D., Wang, Q., Cawood, P. A., Zhao, Z. & Mo, X. Raising the Gangdese Mountains in southern Tibet. *J. Geophys. Res. Solid Earth* **122**, 214–223 (2017).
18. Ibarra, D. E. et al. High-elevation Tibetan Plateau before India–Eurasia collision recorded by triple oxygen isotopes. *Nat. Geosci.* **16**, 810–815 (2023).
19. Scott, E. M. et al. Andean surface uplift constrained by radiogenic isotopes of arc lavas. *Nat. Commun.* **9**, 969 (2018).
20. Dewey, J. F., Hempton, M. R., Kidd, W. S. F., Saroglu, F. & Şengör, A. M. C. Shortening of continental lithosphere: the neotectonics of Eastern Anatolia – a young collision zone. *Geol. Soc. Lond. Spec. Publ.* **19**, 1–36 (1986).
21. Reilinger, R. et al. GPS constraints on continental deformation in the Africa-Arabia-Eurasia continental collision zone and implications for the dynamics of plate interactions. *J. Geophys. Res. Solid Earth* **111**, B5411 (2006).
22. Gök, R., Pasyanos, M. E. & Zor, E. Lithospheric structure of the continent-continent collision zone: eastern Turkey. *Geophys. J. Int* **169**, 1079–1088 (2007).
23. Zhu, H. High Vp/Vs ratio in the crust and uppermost mantle beneath volcanoes in the central and eastern Anatolia. *Geophys. J. Int.* **214**, 2151–2163 (2018).
24. Al-Lazki, A. I. et al. Tomographic Pn velocity and anisotropy structure beneath the Anatolian plateau (eastern Turkey) and the surrounding regions. *Geophys. Res. Lett.* **30**, 8043 (2003).
25. Mutlu, A. K. & Karabulut, H. Anisotropic Pn tomography of Turkey and adjacent regions. *Geophys. J. Int.* **187**, 1743–1758 (2011).
26. Artemieva, I. M. & Shulgin, A. Geodynamics of Anatolia: Lithosphere thermal structure and thickness. *Tectonics* **38**, 4465–4487 (2019).
27. Keskin, M. Magma generation by slab steepening and breakoff beneath a subduction-accretion complex: An alternative model for collision-related volcanism in Eastern Anatolia, Turkey. *Geophys. Res. Lett.* **30**, 8046 (2003).
28. Schleiffarth, W. K., Darin, M. H., Reid, M. R. & Umhoefer, P. J. Dynamics of episodic Late Cretaceous–Cenozoic magmatism across Central to Eastern Anatolia: New insights from an extensive geochronology compilation. *Geosphere* **14**, 1990–2008 (2018).
29. Şengör, A. M. C., Özeren, S., Genç, T. & Zor, E. East Anatolian high plateau as a mantle-supported, north-south shortened domal structure. *Geophys. Res. Lett.* **30**, 8045 (2003).
30. Zor, E. et al. The crustal structure of the East Anatolian plateau (Turkey) from receiver functions. *Geophys. Res. Lett.* **30**, 8044 (2003).
31. Zhou, Z., Thybo, H., Tang, C., Artemieva, I. & Kusky, T. Test of P-wave receiver functions for a seismic velocity and gravity model across the Baikal Rift Zone. *Geophys. J. Int.* **232**, 176–189 (2023).
32. Sandvol, E., Turkelli, N. & Barazangi, M. The Eastern Turkey Seismic Experiment: The study of a young continent-continent collision. *Geophys. Res. Lett.* **30**, 8038 (2003).
33. Medved, I., Polat, G. & Koulakov, I.Crustal Structure of the Eastern Anatolia Region (Turkey) based on seismic tomography. *Geosciences* **11**, https://doi.org/10.3390/geosciences11020091 (2021).
34. Lei, J. & Zhao, D. Teleseismic evidence for a break-off subducting slab under Eastern Turkey. *Earth Planet. Sci. Lett.* **257**, 14–28 (2007).
35. Türkoğlu, E., Unsworth, M., Çağlar, İ., Tuncer, V. & Avşar, Ü. Lithospheric structure of the Arabia-Eurasia collision zone in eastern Anatolia: Magnetotelluric evidence for widespread weakening by fluids. *Geology* **36**, 619–622 (2008).
36. Tanış, T., Sarı, A. & Seyitoğlu, G. 3D seismic reflection evidence of the blind thrust system in the northern Diyarbakır, southeast Turkey. *Arab. J. Geosci.* **15**, 726 (2022).
37. Caldwell, W. B., Klemperer, S. L., Lawrence, J. F., Rai, S. S. & Ashish Characterizing the Main Himalayan Thrust in the Garhwal Himalaya, India with receiver function CCP stacking. *Earth Planet. Sc. Lett.* **367**, 15–27 (2013).
38. Yin, A. & Harrison, T. M. Geologic evolution of the Himalayan-Tibetan orogen. *Annu. Rev. Earth Pl. Sc.* **28**, 211–280 (2000).
39. Förste, C. et al. EIGEN-6C4: The latest combined global gravity field model including GOCE data up to degree and order 2190. *GFZ Potsdam GRGS Toulouse* https://doi.org/10.5880/icgem.2015.1 (2014).

40. Ward, K. M., Zandt, G., Beck, S. L., Christensen, D. H. & McFarlin, H. Seismic imaging of the magmatic underpinnings beneath the Altiplano-Puna volcanic complex from the joint inversion of surface wave dispersion and receiver functions. *Earth Planet. Sc. Lett.* **404**, 43–53 (2014).
41. Comeau, M. J., Unsworth, M. J., Ticona, F. & Sunagua, M. Magnetotelluric images of magma distribution beneath Volcan Uturuncu, Bolivia; implications for magma dynamics. *Geology* **43**, 243–246 (2015).
42. Takei, Y. Effect of pore geometry on $V_P/V_S$: From equilibrium geometry to crack. *J. Geophys. Res. Solid Earth* **107**, https://doi.org/10.1029/2001JB000522 (2002).
43. Iwamori, H. et al. Simultaneous analysis of seismic velocity and electrical conductivity in the crust and the uppermost mantle: A forward model and inversion test based on grid search. *J. Geophys. Res. Solid Earth* **126**, e2021JB022307 (2021).
44. Sato, H., Sacks, I. S. & Murase, T. The use of laboratory velocity data for estimating temperature and partial melt fraction in the low velocity zone: comparison with heat flow and electrical conductivity studies. *J. Geophys. Res. Solid Earth* **94**, 5689–5704 (1989).
45. Özacar, A. A., Zandt, G., Gilbert, H. & Beck, S. L. Seismic images of crustal variations beneath the East Anatolian Plateau (Turkey) from teleseismic receiver functions. *Geol. Soc. Lond. Spec. Publ.* **340**, 485–496 (2010).
46. Thybo, H. & Nielsen, C. A. Magma-compensated crustal thinning in continental rift zones. *Nature* **457**, 873–876 (2009).
47. Thybo, H. & Artemieva, I. M. Moho and magmatic underplating in continental lithosphere. *Tectonophysics* **609**, 605–619 (2013).
48. Vielzeuf, D. & Schmidt, M. W. Melting relations in hydrous systems revisited; application to metapelites, metagreywackes and metabasalts. *Contrib. Mineral. Petr.* **141**, 251–267 (2001).
49. Huang, W. L. & Wyllie, P. J. Melting relations of muscovite-granite to 35 kbar as a model for fusion of metamorphosed subducted oceanic sediments. *Contrib. Mineral. Petr.* **42**, 1–14 (1973).
50. Kounoudis, R. et al. Seismic tomographic imaging of the Eastern Mediterranean Mantle: Implications for terminal-stage subduction, the uplift of anatolia, and the development of the North Anatolian Fault. *Geochem. Geophys. Geosyst.* **21**, e2020GC009009 (2020).
51. Schulte-Pelkum, V. et al. Imaging the Indian subcontinent beneath the Himalaya. *Nature* **435**, 1222–1225 (2005).
52. Wittlinger, G., Farra, V., Hetényi, G., Vergne, J. & Nábělek, J. Seismic velocities in Southern Tibet lower crust: a receiver function approach for eclogite detection. *Geophys. J. Int* **177**, 1037–1049 (2009).
53. Hetényi, G. et al. Density distribution of the India plate beneath the Tibetan plateau: Geophysical and petrological constraints on the kinetics of lower-crustal eclogitization. *Earth Planet. Sc. Lett.* **264**, 226–244 (2007).
54. Horne, A. V., Sato, H. & Ishiyama, T. Evolution of the Sea of Japan back-arc and some unsolved issues. *Tectonophysics* **710–711**, 6–20 (2017).
55. Molnar, P. & England, P. Late Cenozoic uplift of mountain ranges and global climate change: chicken or egg? *Nature* **346**, 29–34 (1990).
56. Lamb, S. & Davis, P. Cenozoic climate change as a possible cause for the rise of the Andes. *Nature* **425**, 792–797 (2003).
57. Zhu, D. et al. Interplay between oceanic subduction and continental collision in building continental crust. *Nat. Commun.* **13**, 7141 (2022).
58. Ligorria, J. P. & Ammon, C. J. Iterative deconvolution and receiver-function estimation. *B. Seismol. Soc. Am.* **89**, 1395–1400 (1999).
59. Park, J. & Levin, V. Receiver functions from multiple-taper spectral correlation estimates. *B. Seismol. Soc. Am.* **90**, 1507–1520 (2000).
60. Tkalčić, H. et al. Multistep modelling of teleseismic receiver functions combined with constraints from seismic tomography: crustal structure beneath southeast China. *Geophys. J. Int.* **187**, 303–326 (2011).
61. Zhu, L. & Kanamori, H. Moho depth variation in southern California from teleseismic receiver functions. *J. Geophys. Res.* **105**, 2969–2980 (2000).
62. Ammon, C. J., Randall, G. E. & Zandt, G. On the nonuniqueness of receiver function inversions. *J. Geophys. Res.* **95**, 15303–15318 (1990).
63. Akuhara, T., Tsuji, T. & Tonegawa, T. Overpressured underthrust sediment in the Nankai Trough forearc inferred from transdimensional inversion of high-frequency teleseismic waveforms. *Geophys. Res. Lett.* **47**, https://doi.org/10.1029/2020GL088280 (2020).
64. Sambridge, M. Geophysical inversion with a neighborhood algorithm—I. Searching a parameter space. *Geophys. J. Int.* **138**, 479–494 (1999).
65. Sambridge, M. Geophysical inversion with a neighborhood algorithm—II, Appraising the ensemble. *Geophys. J. Int.* **138**, 727–746 (1999).
66. Amante, C. & Eakins, B. W. ETOPO1 1 arc-minute global relief model: procedures, data sources and analysis. *Commerce, Boulder, CO, USA: National Geophysical Data Center, NESDIS, NOAA, U.S. Dept.* https://doi.org/10.7289/V5C8276M (2009).
67. Eyuboglu, Y., Dudas, F. O., Zhu, D., Liu, Z. & Chatterjee, N. Late Cretaceous I- and A-type magmas in eastern Turkey: Magmatic response to double-sided subduction of Paleo- and Neo-Tethyan lithospheres. *Lithos* **326-327**, 39–70 (2019).
68. Topuz, G., Candan, O., Zack, T. & Yılmaz, A. East Anatolian plateau constructed over a continental basement: No evidence for the East Anatolian accretionary complex. *Geology* **45**, 791–794 (2017).
69. Wyllie, P. J. The origin of kimberlite. *J. Geophys. Res.* **85**, 6902–6910 (1980).
70. Wyllie, P. J. Experimental petrology of upper mantle materials, processes and products. *J. Geodyn.* **20**, 429–468 (1995).
71. Pritchard, M. E. & Gregg, P. M. Geophysical evidence for silicic crustal melt in the continents; Where, what kind, and how much? *Elements* **12**, 121–127 (2016).
72. Wang, G., Thybo, H. & Artemieva, I. M. No mafic layer in 80 km thick Tibetan crust. *Nat. Commun.* **12**, 1069 (2021).


## Acknowledgements

This project is supported by the National Natural Science Foundation of China (No. 92055210 to HT & IA, No. 91755213 to TK), the Basic Research Fund from CAGS, China (Lithospheric Structure and Geodynamic Processes 2023 to HT & IA), the MOST Special Fund from the State Key Laboratory of GPMR of CUG-Wuhan, China (No. GPMR2019010), and TÜBITAK grant, Turkey (No. 1199B472000709 to HT). We thank Hayrullah Karabulut and the Kandilli Observatory in Istanbul, Turkey for helping with accessing part of the seismic data, and Irina Medved for generating the tomographic profiles based on ref. 33.

## Author contributions

H.T., I.M.A. and T.K. conceived the project to compare different segments of the Tethys belts from geological and geophysical observations. Z.Z. processed the seismic data under supervision by H.T. and C.T., other geophysical and geological data were integrated by Z.Z. under supervision by H.T., I.M.A. and T.K. The interpretation was developed by H.T., I.M.A. and Z.Z. in numerous discussions of the results and their implications. All authors contributed to writing the paper.

## Competing interests

The authors declare no competing interests.

## Additional information

**Supplementary information** The online version contains supplementary material available at https://doi.org/10.1038/s41467-024-53435-7.

**Correspondence** and requests for materials should be addressed to Hans Thybo or Irina M. Artemieva.

**Peer review information** *Nature Communications* thanks Di-Cheng Zhu, and the other, anonymous, reviewer(s) for their contribution to the peer review of this work. A peer review file is available.

**Reprints and permissions information** is available at http://www.nature.com/reprints

**Publisher's note** Springer Nature remains neutral with regard to jurisdictional claims in published maps and institutional affiliations.

**Open Access** This article is licensed under a Creative Commons Attribution-NonCommercial-NoDerivatives 4.0 International License, which permits any non-commercial use, sharing, distribution and reproduction in any medium or format, as long as you give appropriate credit to the original author(s) and the source, provide a link to the Creative Commons licence, and indicate if you modified the licensed material. You do not have permission under this licence to share adapted material derived from this article or parts of it. The images or other third party material in this article are included in the article's Creative Commons licence, unless indicated otherwise in a credit line to the material. If material is not included in the article's Creative Commons licence and your intended use is not permitted by statutory regulation or exceeds the permitted use, you will need to obtain permission directly from the copyright holder. To view a copy of this licence, visit http://creativecommons.org/licenses/by-nc-nd/4.0/.

© The Author(s) 2024